Inter-basin and Multi-time Scale Interactions in generating the 2019

Extreme Indian Ocean Dipole

3 Lei Zhang^{1*}, Weiqing Han¹, Zeng-Zhen Hu²

- ¹Department of Atmospheric and Oceanic Sciences, University of Colorado, Boulder, Colorado, USA.
- ²Climate Prediction Center, NCEP/NWS/NOAA 5830 University Research Court, College Park, MD
- 6 20740, USA

1

2

Revised manuscript submitted to Journal of Climate

- **8** *Corresponding author:
- 9 Lei Zhang

- 10 Department of Atmospheric and Oceanic Sciences,
- 11 University of Colorado, Boulder, CO 80302, USA
- 12 **Email:** lezh8230@colorado.edu

13 Abstract

An unprecedented extreme positive Indian Ocean Dipole event (pIOD) occurred in 2019, which has caused widespread disastrous impacts on countries bordering the Indian Ocean, including the East African floods and vast bushfires in Australia. Here we investigate the causes for the 2019 pIOD by analyzing multiple observational datasets and performing numerical model experiments. We find that the 2019 pIOD is triggered in May by easterly wind bursts over the tropical Indian Ocean associated with the dry phase of the boreal summer intraseasonal oscillation, and sustained by the local atmosphere-ocean interaction thereafter. During September-November, warm sea surface temperature anomalies (SSTA) in the central-western tropical Pacific further enhance the Indian Ocean's easterly winds, bringing the pIOD to an extreme magnitude. The central-western tropical Pacific warm SSTA is strengthened by two consecutive Madden Julian Oscillation (MJO) events that originate from the tropical Indian Ocean. Our results highlight the important roles of cross-basin and cross-timescale interactions in generating extreme IOD events. The lack of accurate representation of these interactions may be the root for a short lead time in predicting this extreme pIOD with a state-of-the-art climate forecast model.

Keywords: Indian Ocean Dipole; Inter-basin interaction; Intraseasonal oscillation; Climate prediction;

1. Introduction

The Indian Ocean Dipole (IOD) is the dominant mode of Indian Ocean interannual climate variability (Saji et al. 1999; Webster et al. 1999), which is characterized by opposite sea surface temperature anomalies (SSTAs) between the eastern Indian Ocean off the coast of Sumatra and the western tropical Indian Ocean. A positive phase of IOD (pIOD) event is associated with warming in the western and cooling in the eastern Indian Ocean, accompanied by surface easterly wind anomalies over the tropical Indian Ocean (Fig. 1). Reversed conditions hold for a negative phase of IOD. The IOD events have profound influences on weather and climate in surrounding countries, including Indian summer monsoon variability (Ashok et al. 2004; Kripalani and Kumar 2004; Gadgil et al. 2004; Ashok and Saji 2007), flood and drought over East Africa and Indonesia (Clark et al. 2003; Black et al. 2002), and temperature and rainfall anomalies in Australia (Cai et al., 2009; Cai et al., 2011; Li et al., 2016; Saji and Yamagata, 2003). Through atmospheric teleconnection and interactions with the tropical Pacific Ocean, footprints of IOD can be found worldwide (Saji and Yamagata 2003; Behera and Yamagata 2003; Izumo et al. 2010; Stuecker et al. 2017; Annamalai et al. 2005; Luo et al. 2010).

The development of the IOD involves large-scale ocean-atmosphere interactions over the tropical Indian Ocean (Murtugudde et al. 2000; Li et al. 2003; Lau and Nath 2004). During a pIOD, the SSTA pattern with warming in the west and cooling in the east drives surface southeasterly/easterly wind anomalies over the eastern/central tropical Indian Ocean through changes in the zonal sea level pressure (SLP) gradient (Lindzen and Nigam 1987) (Fig. S1). The southeasterly wind anomalies along the Sumatra and Java coasts, in turn, cause offshore Ekman currents that diverge from the coasts, allowing the colder subsurface water to upwell to the ocean surface and thus enhance SST cooling. Meanwhile, the anomalous winds enhance the southeasterly trades and surface evaporation, further strengthening the SST cooling signals. Along the equator, easterly wind components cause westward surface currents, transporting the

warm pool water from the eastern Indian Ocean westward and amplifying the SSTA zonal gradient; concurrently, easterly wind anomalies induce Ekman divergence (upwelling) along the equator, and Ekman convergence (downwelling) off the equator. The upwelling (downwelling) signals propagate eastward (westward) as equatorial Kelvin (Rossby) waves, further enhancing the east-west dipole pattern of SSTA (Gualdi et al. 2003; Feng and Meyers 2003; Shinoda et al. 2004; Huang and Shukla 2007a).

In addition to the local ocean-atmosphere interaction, the El Niño-Southern Oscillation (ENSO), which is the dominant interannual climate mode of variability on the planet (McPhaden et al. 2006; Huang and Shukla 2007a, b; Huang and Kinter III 2002), can also play a role in the IOD formation (Saji et al. 2006; Allan et al. 2003; Krishnamurthy and Kirtman 2003; Annamalai et al. 2003; Meyers et al. 2007; Huang and Shukla 2007a; Wang et al. 2019; Huang and Kinter III 2002). During El Niño (the positive phase of ENSO), convection (rainfall) is suppressed over the western tropical Pacific warm pool and the Maritime Continent (Fig. S2), leading to higher SLP in the region (Fig. S1). The zonal SLP gradient induces surface easterly wind anomalies over the tropical Indian Ocean and thereby contributes to the generation and development of the pIOD.

Since the early 1980s when satellite observations became available, three extreme pIOD events have occurred in 1994, 1997, and 2006 (Fig. 1), which have been extensively studied (Saji et al. 1999; Webster et al. 1999; Behera et al. 1999; Vinayachandran et al. 1999; Horii et al. 2008). The three extreme pIOD events are all accompanied by El Niño, though of different flavors of ENSO with major warm SSTA located at different regions of the tropical Pacific Ocean; while both 1997 and 2006 are classified as the eastern Pacific El Niño, 1994 is a central Pacific El Niño event (Yu et al. 2012). Using an atmospheric general circulation model (AGCM) forced with observed Pacific SSTAs in 1994, 1997, and 2006, we indeed find that the El Niño events induce easterly wind anomalies over the tropical Indian Ocean and thereby strengthen the three historical extreme pIOD events (Fig. S3).

In fall 2019, another extreme pIOD occurred with the peak value of the monthly dipole mode index (DMI, defined as the west-east SST gradient in the tropical Indian Ocean) close to 2.2 °C (Fig. 1f). This makes the 2019 pIOD the strongest event during the satellite era since the early 1980s (Fig. 1e). Meanwhile, positive SSTAs are observed in the central tropical Pacific – particularly the central-western Pacific west of the dateline – in 2019, with the center of warming being shifted to the further west compared to that during the other three extreme pIOD events (Fig. 1). This 2019 extreme pIOD caused disastrous impacts on countries nearby. For instance, rainfall at the horn of Eastern Africa is up to 300% above average in October-November 2019 (Famine Early Warning Systems Network report, https://reliefweb.int/report/south-sudan/east-africa-food-security-outlook-high-food-assistance-needspersist-food), when the pIOD attains its peak. The excess rainfall results in severe flooding in the region that killed hundreds and affected more than 2.8-million people (United Nations Office for the Coordination of Humanitarian Affairs report, https://reliefweb.int/report/south-sudan/eastern-africaregion-regional-flood-snapshot-november-2019). Meanwhile, massive bushfires raged through Australia due to the warm and dry conditions there, which are typically observed during pIOD events and therefore are likely associated with the 2019 pIOD. The 2019 pIOD also contributed to the extremely warm conditions over East Asia during the winter season of 2019-2020 (Doi et al. 2020a). Therefore, understanding the generation, development, and predictability of the 2019 extreme pIOD event has large societal benefits.

2. Data and Method

74

75

76

77

78

79

80

81

82

83

84

85

86

87

88

89

90

91

92

93

94

95

96

2.1 Observational data sets

In this study, we use the monthly SST data from the Hadley Centre Sea Ice and SST (HadISST) (Rayner et al. 2003) and Extended Reconstructed SST version 5 (ERSSTv5) (Huang et al., 2017) during 1979-2019, and National Oceanic and Atmospheric Administration (NOAA) Optimum Interpolation SST

version 2 (OISSTv2) (Reynolds et al. 2002) during 1982-2019 to analyze the tropical Indian Ocean and Pacific SSTAs during the extreme pIODs. To analyze the seasonal variations of the tropical Indo-Pacific atmospheric conditions, we use monthly surface wind, sea level pressure, and precipitation data from European Centre for Medium-Range Weather Forecasts (ECMWF) Reanalysis 5 (ERA5) (Hersbach et al. 2019), and outgoing longwave radiation (OLR) data from NOAA Interpolated OLR (Liebmann and Smith 1996). To examine the subseasonal variations and their contributions to the 2019 pIOD, we analyze daily OISSTv2 and ERA5 surface wind data, for which we remove the first three harmonics of the daily climatology to obtain the anomaly fields. To examine the oceanic wave processes, we also analyzed satellite-derived daily sea surface height (SSH) data during 1993-2019 obtained from Copernicus Marine Environment Monitoring Service (CMEMS).

97

98

99

100

101

102

103

104

105

106

107

108

109

110

111

112

113

114

115

116

117

118

119

To examine the Madden-Julian Oscillation (MJO) activities, we use an MJO index from Climate Prediction Center (CPC), National Centers for Environmental Prediction (NCEP), NOAA, which is based extended empirical orthogonal function analysis available on an and at https://www.cpc.ncep.noaa.gov/products/precip/CWlink/daily mjo index/mjo index.shtml. For comparison, we also use the OLR-based MJO index (OMI) (Kiladis et al. 2014) available at https://www.esrl.noaa.gov/psd/mjo/mjoindex/.

To select the extreme pIOD events during the satellite era, we use the DMI (Saji et al. 1999), which is differences of SSTAs averaged over (50°E–70°E; 10°S–10°N) and (90°E–110°E; 10°S–EQ). The extreme pIODs are defined as the year when the monthly DMI during the peak season (September to November) exceeds two standard deviations of the index (~1°C). Four pIOD events are selected, which are 1994, 1997, 2006, and 2019.

To explore the causes for the SSTAs associated with the 2019 pIOD, we examine the oceanic mixed layer (OML) heat budget. Following Huang et al. (2010), the heat budget equation of OML is

 $T_t = Q_u + Q_v + Q_w + Q_{zz} + Q_q$

where T_t is the time tendency of the OML temperature, Q_u and Q_v represent the zonal and meridional advection, Q_w and Q_{zz} are the vertical entrainment and vertical diffusion, and Q_q is the net surface heat flux. Monthly heat budget terms are diagnosed using outputs from the NCEP Global Ocean Data Assimilation System (GODAS) (Ji et al. 1998; Huang et al. 2010), in which the mixed layer depth is defined as the depth at which the density difference from the surface reaches 0.125 kg m⁻³. Note that there are relatively large biases in the Q_w and Q_{zz} terms for the coastal area due to the limited resolution, and therefore their contributions to the cold pole of the pIOD in the eastern tropical Indian Ocean may not be well captured.

2.2 CFSv2 forecasts

To assess the prediction skill of IOD, we verify the real-time predictions of the Climate Forecast System version 2 (CFSv2) (Xue et al. 2013; Saha et al. 2014), which is a global coupled climate model and provides real-time operational forecasts at the National Centers for Environmental Prediction. In this study, we analyze the 9-month predictions starting from January through September 2019, and the forecasts were initiated with 40-day initiation conditions (from 10th of the target month going backward to the previous month for 40 days), and 4 forecasts each day (0000, 0600, 1200, and 1800 UTC). Hence, we use 160 ensemble members to construct the ensemble mean in each month.

2.3 Atmosphere model

To investigate the impact of the Pacific forcing on the tropical Indian Ocean through the atmospheric bridge, we perform two sets of sensitivity experiments using the AGCM ECHAM4.6 (Roeckner et al. 1996) from Max Planck Institute (MPI) in Hamburg (HAM), which is a branch from the ECMWF. The model horizontal resolution is approximately 2.8°, with 19 vertical levels. For each

experiment, the model is integrated for 40 years, and the first four years are discarded given that it takes a few years to reach the model equilibrium. Hence, we have a 36-member ensemble for all the experiments.

In addition to the control run, which is forced with monthly SST climatology, we perform two sets of experiments, forced with realistic and idealized Pacific SSTA, respectively. In the first set of experiments, we add September-November averaged tropical Pacific SSTA (30°N-30°S) during the extreme pIODs to the monthly SST climatology throughout the year. We perform three experiments, forced with observed 1994/2006 (average of the two events, since both years exhibit similar central tropical Pacific warming anomalies), 1997 and 2019 Pacific SSTA, respectively.

In the second set of experiments, we force the model with idealized SST warming anomalies centered at the CP-I (140°E-170°W, 10°S-10°N), CP-II (170°E-140°W, 10°S-10°N) and the eastern tropical Pacific (EP; 160°W-80°W, 10°S-10°N). To examine whether the western (WNP; 125°E-165°E, 10°N-30°N) and eastern (ENP; 160°W-120°W, 10°N-30°N) North Pacific SST warming in 2019 also contributes to the development of the extreme pIOD, we perform two additional experiments by adding idealized SST warming in those two regions separately. The idealized SST warming has a 1°C peak warming at the center and gradually decays to 0°C toward the edges. Since the eastern Pacific warming in 1997 is much stronger compared with those in the other extreme pIOD years (Fig. 1), we perform another additional experiment with 2 °C peak warming centered in the eastern tropical Pacific region.

2.4 Linear ocean model

To investigate the relative roles of remote and local wind forcings in affecting the coastal ocean off the Sumatra and Java coasts, we use a linear continuously stratified ocean model (McCreary 1981; Han 2005), forced with differences of Indian Ocean surface winds between the CP-I warm SSTA and the control run of AGCM experiments. The model domain is approximately 30°E-120°E and 35°S-35°N. The ocean model experiment started from a state of rest with a realistic background stratification and 25

baroclinic modes. The ocean bottom is assumed to be flat with a depth of 4000 m, and the horizontal resolution is 0.5°. The model is integrated for 60 months, and the last 48-month results are analyzed.

3. The extreme pIOD in 2019

165

166

167

168

169

170

171

172

173

174

175

176

177

178

179

180

181

182

183

184

185

186

187

Here we examine the evolution of the extreme pIOD in 2019 (Figs. 2, 3) and explore the associated physical mechanisms. Observations show that the 2019 pIOD starts to develop in May (Figs. 1f, 2b), as seen from the dramatic increase in the DMI with an amplitude larger than 1°C in mid-May, which is mainly associated with strong warming in the western tropical Indian Ocean – the western pole of the pIOD (Fig. 2b). We also find warm SSTAs in the tropical Indian Ocean before May (Fig. 2b), which are mainly located at the southern tropical Indian Ocean in the so-called Seychelles-Chagos thermocline ridge region (Fig. 6), and therefore these warm signals may not be part of the pIOD signals. An OML budget analysis reveals that the Indian Ocean SSTA dipole in May is primarily caused by changes in the surface heat fluxes (Fig. 4a). Consistently, the Hovmöller diagram of zonal wind anomalies (Fig. 2a) shows that episodical easterly wind burst (EWBs) prevail over the western and central Indian Ocean basin in the early and mid-May, weakening the westerly monsoon circulation, reducing the surface turbulent heat loss from the ocean and thereby causing warm SSTA in the pIOD's western pole. Meanwhile, the EWBs also cause an oceanic upwelling Kelvin wave in the central tropical Indian Ocean that subsequently propagate eastward (Fig. 3). Although the associated zonal SSH gradient anomaly along the Indian Ocean equator is weak averaged in May (Fig. 3), our analysis of temporal evolution shows a delayed impact of the EWBs on SSHA and SSTA in the eastern pole of the pIOD from late May to mid-June, reducing SSHA and SSTA in the region (Figs. 2a-2b, 3 and 5). This is consistent with the further strengthening of the cold pole in late May-early June (Fig. 6). However, since the OML heat budget has relatively large biases in the coastal region, it may not capture the role of oceanic Kelvin waves in enhancing the cold pole (Fig. 4b). Also note that Fig. 2 shows SSTA averaged in the tropical Indian Ocean between 10°S and 10°N,

which underestimates the amplitude of the IOD cold pole that is mainly confined in the coastal region (Fig. 6).

The EWBs are associated with prominent dry anomalies over the eastern tropical Indian Ocean, and both the wind and rainfall anomalies exhibit evident northward propagation (Fig. 5). In late May, the EWBs and the associated dry anomalies reach the North Indian Ocean; meanwhile, wet anomalies accompanied by westerly wind anomalies appear over the tropical Indian Ocean. These northward-propagating intraseasonal variabilities have been extensively studied, and are referred to as the boreal summer intraseasonal oscillation (BSISO) (Lawrence and Webster 2002). Hence, the initiation of the pIOD in May 2019 is triggered by the EWBs associated with the dry phase of the BSISO, which cause dipole-like SSTA in the tropical Indian Ocean with a few days lag (Fig. 6) through changing the surface heat fluxes.

Once the EWBs induce east-west dipole-like SSTAs in the tropical Indian Ocean in May, local positive atmosphere-ocean feedback kicks-off, which sustains the development of both SST and wind anomalies associated with the pIOD in the following months. Indeed, the DMI remains positive, and easterly wind anomalies prevail throughout June and July, despite slightly weaker amplitudes compared to May. From late July to October, the pIOD exhibits a steady intensification with a temporary weakening in early September (Figs. 1f, 2c), and the zonal SSH gradient strengthens (Fig. 3). The monthly DMI increases from 0.7°C in July to 2.2°C in October when the pIOD peaks, making it the strongest event in the past ~40 years. Consistently, easterly wind anomalies intensify and occupy the entire equatorial basin in October (Fig. 2a), which also cause equatorial and coastal upwelling Kelvin waves propagating from the central equatorial Indian Ocean to the Sumatra and Java coasts (Fig. 3). The temporary interruption of the pIOD development in early September is due to the influences of the MJO (Madden and Julian 1971) (Fig. S4). As revealed by multiple MJO indices, a wet MJO event originated from the tropical Indian

Ocean in late August and subsequently propagate eastward into the tropical Pacific. The wet MJO is associated with strong intraseasonal westerly wind anomalies, which temporarily disrupt the growth of the 2019 pIOD.

4. Pacific contribution to the extreme pIOD

The unprecedented intensity of the 2019 pIOD is due to a combination of the large initial warming in the western pole in May and the persistent intensification during August-October. While the former is caused by a strong dry BSISO event, what causes the intensification of easterly wind anomalies and the pIOD in August-October 2019 demands further investigation. Previous studies have shown that active inter-basin interactions between the tropical Indian and Pacific Oceans play important roles in affecting tropical climate variability (Wang 2019; Cai et al. 2019; Zhang and Han 2018; Luo et al. 2012; Han et al. 2014; Zhang et al. 2019). Note that the development of the 2019 pIOD in boreal summer and fall is accompanied by persistent positive SSTAs in the central tropical Pacific, with a maximum magnitude exceeding 1°C to the west of the dateline where the mean SST exceeds 29 °C (Figs. 1d, 2b). This warming center is shifted further to the west compared to that during the other historical extreme pIODs (Fig. 1).

Do the warm SSTAs within the central-western Pacific contribute to the development of the 2019 pIOD? To answer this question, we perform AGCM experiments forced with observed September-November (SON) mean SSTAs of 2019 in the tropical Pacific (Figs. S3e, S3f). Results show that the central-western tropical Pacific warming in 2019 shifts the tropical Pacific convection center eastward and thereby suppresses convection over the Maritime Continent. Thus, the warm SSTAs in the central-western tropical Pacific indeed enhance the easterly wind anomalies over the tropical Indian Ocean, contributing to the pIOD development in 2019. Interestingly, we note that the Pacific SSTA also induces cyclonic wind anomalies over the western North Pacific (Fig. S3f), which agrees with the observations

(Fig. S1d) and the associated northerly wind anomalies over East Asia have been suggested to contribute to the severe drought in East China in 2019 (Ma et al. 2020). This further validates our model results.

233

234

235

236

237

238

239

240

241

242

243

244

245

246

247

248

249

250

251

252

253

254

255

Hence, the development of the 2019 pIOD and the three historical extreme pIOD events are all influenced by the tropical Pacific forcing. However, the tropical Pacific warming anomalies are centered at different locations during the four pIOD events. Are the responses in the tropical Indian Ocean sensitive to the location of the tropical Pacific warming? To explore the relative roles of the Pacific SSTAs at different locations on the development of the four extreme pIOD events, we conduct another set of AGCM experiments using idealized SSTA forcing (Fig. 7). Positive SSTAs with the same 1°C maximum warming at the center are specified for different areas of the Pacific basin to represent the observed Pacific SSTAs during the four extreme pIODs. Here we use CP-I to represent the location of the central-western tropical Pacific warming during 2019, which is to the west of the dateline; as a comparison, CP-II represents the location of Central Pacific El Niños during 1994 and 2006, with the warming center located to the east of the dateline. Results show that the anomalous warming in the tropical Pacific induces easterly wind anomalies in the tropical Indian Ocean, no matter the warming is in the CP-I, CP-II, or eastern tropical Pacific region (Figs. 7a–c). The role of the Pacific warm SSTA in causing tropical Indian Ocean easterly wind anomalies is mainly through shifting the Pacific convection center eastward and thereby causing below-average rainfall over the Maritime Continent (Fig. S5), which in turn induces atmospheric Rossby waves to its west over the Indian Ocean manifested as a pair of low-level anomalous anti-cyclones straddling the equator that correspond to strong easterly wind anomalies in the tropics.

Interestingly, the intensities of the Indian Ocean easterly wind anomalies driven by the tropical Pacific SSTAs depend critically on the location of the SSTA forcing. While warming in the CP-I region produces the strongest wind anomalies in the equatorial Indian Ocean (Fig. 7a), impacts of the same degree of warming in CP-II and eastern Pacific cold tongue region on the Indian Ocean are relatively weak (Figs.

7a–c, S5). This is due to the nonlinear dependence of the tropical rainfall, which is the heating source that drives changes in atmospheric circulation, on the mean state SST (Gadgil et al. 1984; Graham and Barnett 1987; Waliser and Graham 1993) – the increases of rainfall per degree SST warming (mm day⁻¹ °C⁻¹) is higher in the region where the background SST is higher. Indeed, the positive rainfall anomalies in the tropical Pacific caused by warming in CP-II region are larger than those caused by warming in CP-II region and eastern tropical Pacific (Fig. S5). Therefore, the longitudinal location of tropical Pacific warm SSTA in 2019 provides the most favorable condition for the development of the pIOD.

Note that both the remote equatorial easterlies and the local alongshore southeasterlies off Sumatra and Java coasts can induce coastal upwelling in the eastern pole of the pIOD and thereby favor the pIOD development. However, while the CP-I warming induces strong easterly wind anomalies across the equatorial Indian Ocean which enhance upwelling in the eastern pole via exciting eastward-propagating equatorial Kelvin waves, it causes weak but southwesterly winds off Sumatra and Java coasts which reduce upwelling and weaken the cold SSTA there (Fig. 7a). To assess the relative importance of remote versus local wind anomalies induced by CP-I warm SSTA in affecting the cold SSTA in the east pole of the pIOD, we use the wind anomalies induced by CP-I warm SSTA to force a linear ocean model. The results show that the remote equatorial winds dominate the local winds in driving upwelling cooling in the eastern pole, causing east-west dipole-like SSH anomalies that favor enhancing the pIOD (Fig. 8). Indeed, observations also show eastward propagating Kelvin wave signals originated from the central equatorial Indian Ocean in October 2019 (Fig. 3). These results further support the prominent role of the CP-I warming in enhancing the pIOD, despite the weak alongshore wind response over the eastern Indian Ocean.

Given that the eastern Pacific positive SSTAs during 1997-1998 El Niño are much stronger than those in the other three extreme pIODs (Fig. 1), we performed one additional sensitivity experiment by

doubling the warming magnitude in the eastern tropical Pacific (Fig. 7d). Results show that the Indian Ocean easterly wind anomalies driven by the stronger eastern Pacific warm SSTA with 2°C at the center are as strong as those induced by the CP-I warm SSTA with 1°C at the center (Figs. 7a, d). Consistently, the 1997 pIOD is the second strongest event during the satellite era after the 2019 pIOD.

We also note that in 2019, weak positive SSTAs are seen in the western North Pacific south of Japan, and strong SSTAs are shown in the eastern North Pacific east of the Hawaiian Islands, while these warming signals are absent in the other three historical extreme pIOD years (Fig. 1). We then examine if those SSTAs also contribute to the 2019 pIOD by performing model experiments with idealized warm SSTAs added in the two regions separately. Results show that although the western North Pacific warming induces easterly wind anomalies over the tropical Indian Ocean, its impact is much weaker compared with that of the tropical Pacific warm SSTAs (Figs. 7a-e). The eastern North Pacific warm SSTA almost does not affect the Indian Ocean winds (Fig. 7f). Consequently, it is the warming in the central-western tropical Pacific that enhances the 2019 pIOD and makes it the strongest pIOD in the past ~40 years.

We note that the central Pacific warm SSTA can be found as early as winter 2018-2019 (Doi et al. 2020b), but it decays significantly in spring 2019 and then re-intensifies since July 2019 (Fig. 2b). To explore the causes for the strengthening of the central-western tropical Pacific warm SSTA in the summer and fall of 2019, we carry out a budget analysis of mixed layer temperature (figure not shown). Results show that the SST warming tendency mainly occurred in July and September, and is primarily caused by surface heat flux anomalies, with some contribution from the reduced upwelling and meridional heat advection anomalies. These atmospheric and oceanic anomalies are closely related to the westerly wind anomalies in the region (Fig. 2a), which weaken the wind speed and the oceanic upwelling. Indeed, the pentad-mean anomalies in the two months show intraseasonal westerly wind anomalies that sustain for 3-4 pentads, which are followed by SST warming tendency (not shown). As shown in various MJO indices,

the westerly wind bursts in the western tropical Pacific that further strengthen CP-I warm SSTA since July 2019 are associated with two wet MJO events originated from the tropical Indian Ocean (Fig. S4). Hence, the inter-basin and multi-time scale interactions play a crucial role resulting in the 2019 extreme pIOD.

5. Prediction of 2019 extreme pIOD

Given that the 2019 extreme pIOD had large societal impacts, it is meaningful to evaluate the performance of climate models in predicting this event. Here we verify the real-time forecasts from the NCEP CFSv2 (Xue et al. 2013; Saha et al. 2014). The 9-month forecasts starting from January through September 2019 generally call a quick decay of the pIOD in 2019 (Fig. 9), and therefore, it is unsuccessful to predict the extreme pIOD event. Even with initialization in July, which is close to the pIOD peak in October, the forecasts still severely underestimate the DMI amplitude (Fig. 9h). Only when the forecast is initialized in August that the predicted DMI is comparable to the observation (Fig. 9i).

One of the reasons that the model is unsuccessful in predicting the 2019 extreme pIOD is likely due to the interruption of subseasonal activities, which is unpredictable beyond a couple of weeks (Lim et al. 2018). The subseasonal variabilities associated with the BSISO and MJO activities are considered as noises that degrade the predictability of monthly and seasonal climate. As shown above, the BSISO/MJO activities are active in 2019 and play a crucial role in triggering the pIOD and the central tropical Pacific warm SSTA, which subsequently enhances the pIOD. Consequently, the model's ability in predicting the development of the pIOD in 2019 is limited.

We further note that for the forecasts starting in September, the ensemble mean DMI is close to the observed value, but there exists a relatively large spread (Fig. 9i); some members overestimate the DMI while some members underestimate it. A comparison between these two categories shows remarkable differences in the tropical Pacific SST; the mean of the ensemble members that predict a

stronger pIOD also predicts larger SSTAs in the central-western tropical Pacific, as well as in the western and eastern North Pacific (Fig. 10). Since the AGCM sensitivity experiments have suggested that warm SSTA in the central-western tropical Pacific is the most efficient driver for easterly wind anomalies in the tropical Indian Ocean that strengthen the pIOD (Fig. 7), the real-time forecast results (Fig. 10) provide further evidence for the important role of the central-western tropical Pacific warming in the formation of the 2019 extreme pIOD.

6. Summary and Discussion

324

325

326

327

328

329

330

331

332

333

334

335

336

337

338

339

340

341

342

343

344

345

346

An unprecedented positive IOD event (pIOD) occurred in 2019, which has caused severe climatic impacts on countries nearby. By combining observational analysis and numerical model experiments, we investigate the genesis, evolution, and prediction of this extreme event. We find that the 2019 extreme pIOD is triggered by easterly wind bursts (EWBs) over the tropical Indian Ocean in May, which is associated with the suppressed/dry phase of BSISO (Fig. 11a). The EWBs cause warm SSTA in the western pole of the pIOD (by reducing surface wind and evaporative cooling) and to a lesser degree, cold SSTA in the eastern pole. The east-west SST gradient kicked-off the local atmosphere-ocean coupling that sustains its development thereafter. Since August, the pIOD further intensifies and reaches its peak in October. In addition to local positive air-sea feedback, the warm SSTAs in the central-western tropical Pacific (west of the dateline) generate easterly wind anomalies in the equatorial Indian Ocean, enhancing the pIOD and making it the strongest event during the satellite era since the 1980s (Fig. 11b). The warm SSTA in the central-western Pacific mainly develops since July 2019 due to two consecutive MJO events that originate from the tropical Indian Ocean. In addition to the dry BSISO event in May 2019, Du et al. (2020) recently suggested that the westward propagating oceanic downwelling Rossby waves in the southern tropical Indian Ocean could also help to trigger the 2019 pIOD through inducing warm SSTA in the western basin that drives easterly wind anomalies over the tropical Indian Ocean.

Compared to the historical extreme pIOD events of 1994, 1997, and 2006 in the past 40 years, the 2019 pIOD is unique in a few aspects: It is accompanied by the tropical Pacific warm SSTAs located further to the west, with the center located within the warm pool region compared to the other three events: it is the strongest in magnitude as measured by the dipole mode index with large anomalies in both the west and east poles; and it is triggered by and peaked with strong EWBs. While westerly wind bursts associated with the active/wet phase of MJO have been shown to terminate pIOD and initiate El Niño (Rao and Yamagata 2004; Han et al. 2006), roles of easterly wind anomalies over the tropical Indian Ocean associated with the suppressed /dry phase of BSISO and MJO in affecting pIOD have largely been neglected. Importantly, our results show that tropical Indian Ocean responses to Pacific SSTA are sensitive to the location of the SSTA. The warm SSTA centered in the central-western tropical Pacific to the west of the dateline, like 2019, is the most efficient driver of the extreme pIOD compared with warming further to the east (i.e., central and eastern tropical Pacific) as in the other three extreme pIOD events. A recent study by Lu and Ren (2020) argued that the interhemispheric pressure gradient (IHPG) anomaly associated with high-pressure anomalies over the south Indian Ocean and low-pressure anomalies over the Philippine Sea may help strengthen the southeasterly wind anomalies over the eastern tropical Indian Ocean and thereby contribute to the growth of the 2019 pIOD. Interestingly, we note that our AGCM experiments forced with the 2019 Pacific SSTA also reproduces a somewhat similar SLP anomaly pattern (Fig. S3). Hence, the IHPG, which is suggested to contribute to the formation of the 2019 extreme pIOD, could be partly associated with the central Pacific warm SSTA.

347

348

349

350

351

352

353

354

355

356

357

358

359

360

361

362

363

364

365

366

367

368

369

In addition to the conditions associated with the intraseasonal-interannual variations, the multidecadal and centennial trend in the Indian Ocean SST also seems favorable for the development of the 2019 pIOD. For instance, Wang et al. (2020) found that the strengthening trend of the southerly winds off the Sumatra coasts in the past few decades may contribute to the 2019 pIOD by further reinforcing the pIOD-related alongshore wind anomalies in the eastern basin, which subsequently enhances the cold pole of the 2019 pIOD. Such long-term wind changes could be associated with the anthropogenic global warming effect. Indeed, Cai et al. (2014) projected more frequent extreme pIOD events under global warming due to mean state changes that are more conducive to the development of pIOD events.

Doi et al. (2020) recently suggested that their model could predict the development of the 2019 pIOD. The model predicted the pIOD peaking in September and decaying thereafter, whereas in the observations, the amplitude of the pIOD almost doubles from September to October. As discussed above, the developments of the 2019 pIOD and the central-western tropical Pacific warm SSTA involve active subseasonal activities, which makes it predictable only in a short-range (1-2 months). This is likely the reason why the CFSv2 could not predict the 2019 pIOD event, although it is capable of predicting the pIOD events reasonably well one to two seasons ahead (Zhu et al. 2015b). Indeed, it has been suggested that the predictability of a pIOD event may vary case by case due to different involvement of subseasonal activity, such as the MJO (Zhu et al. 2015a). This highlights the important role of multi-time scale and cross-basin interactions in the variability and predictability of the tropical climate, which deserves further attention in future climate research and prediction.

Acknowledgments

We appreciate the constructive comments and insightful suggestions from three reviewers. L. Z. and W. H. are supported by NSF OCE 1658132, NASA OSTST NNX17AI63G, and NSF AGS 1935279. All observational data used in this study are available online. Atmosphere and ocean model results are available at https://scholar.colorado.edu/concern/datasets/xp68kh20j.

390 **References**

- 391 Allan, R. J., C. J. C. Reason, J. A. Lindesay, and T. J. Ansell, 2003: Protracted' ENSO episodes and
- their impacts in the Indian Ocean region. *Deep. Res. Part II Top. Stud. Oceanogr.*, **50**, 2331–2347,
- 393 https://doi.org/10.1016/S0967-0645(03)00059-6.
- 394 Annamalai, S. P. Xie, J. McCreary, and R. Murtugudde, 2005: Impact of Indian ocean Sea Surface
- Temperature on developing El Niño. *J. Clim.*, **18**, 302–319.
- Annamalai, H., R. Murtugudde, J. Potemra, S. P. Xie, P. Liu, and B. Wang, 2003: Coupled dynamics
- over the Indian Ocean: Spring initiation of the Zonal Mode. *Deep. Res. Part II Top. Stud.*
- 398 Oceanogr., **50**, 2305–2330, https://doi.org/10.1016/S0967-0645(03)00058-4.
- Ashok, K., and N. H. Saji, 2007: On the impacts of ENSO and Indian Ocean dipole events on sub-
- regional Indian summer monsoon rainfall. *Nat. Hazards*, **42**, 273–285,
- 401 https://doi.org/10.1007/s11069-006-9091-0.
- 402 —, Z. Guan, N. H. Saji, and T. Yamagata, 2004: Individual and combined influences of ENSO and
- the Indian Ocean Dipole on the Indian summer monsoon. *J. Clim.*, **17**, 3141–3155,
- 404 https://doi.org/10.1175/1520-0442(2004)017<3141:IACIOE>2.0.CO;2.
- BEHERA, S. K., and T. YAMAGATA, 2003: Influence of the Indian Ocean Dipole on the Southern
- 406 Oscillation. J. Meteorol. Soc. Japan, **81**, 169–177, https://doi.org/10.2151/jmsj.81.169.
- Behera, S. K. K., R. Krishnan, and T. Yamagata, 1999: Unusual ocean-atmosphere conditions in the
- tropical Indian Ocean during 1994. Geophys. Res. Lett., 26, 3001–3004,
- 409 https://doi.org/10.1029/1999GL010434.
- 410 Black, E., J. Slingo, and K. R. Sperber, 2002: An Observational Study of the Relationship between
- Excessively Strong Short Rains in Coastal East Africa and Indian Ocean SST. *Mon. Weather Rev.*,
- 412 **131**, 74–94, https://doi.org/10.1175/1520-0493(2003)131<0074:aosotr>2.0.co;2.
- Cai, W., T. Cowan, and A. Sullivan, 2009: Recent unprecedented skewness towards positive Indian
- Ocean Dipole occurrences and its impact on Australian rainfall. *Geophys. Res. Lett.*, **36**, 1–4,
- 415 https://doi.org/10.1029/2009GL037604.
- Cai, W., P. van Rensch, T. Cowan, and H. H. Hendon, 2011: Teleconnection Pathways of ENSO and the
- 417 IOD and the Mechanisms for Impacts on Australian Rainfall. *J. Clim.*, **24**, 3910–3923,
- 418 https://doi.org/10.1175/2011JCLI4129.1.
- 419 —, A. Santoso, G. Wang, E. Weller, L. Wu, K. Ashok, Y. Masumoto, and T. Yamagata, 2014:
- Increased frequency of extreme Indian ocean dipole events due to greenhouse warming. *Nature*,

- **510**, 254–258, https://doi.org/10.1038/nature13327.
- 422 —, and Coauthors, 2019: Pantropical climate interactions. Science (80-.)., 363,
- 423 https://doi.org/10.1126/science.aav4236.
- 424 Clark, C. O., P. J. Webster, and J. E. Cole, 2003: Interdecadal variability of the relationship between the
- Indian Ocean zonal mode and East African coastal rainfall anomalies. J. Clim., 16, 548–554,
- 426 https://doi.org/10.1175/1520-0442(2003)016<0548:IVOTRB>2.0.CO;2.
- Doi, T., S. K. Behera, and T. Yamagata, 2020a: Wintertime Impacts of the 2019 Super IOD on East
- 428 Asia. *Geophys. Res. Lett.*, **47**, 1–9, https://doi.org/10.1029/2020GL089456.
- 429 —, S. K. Behera, and T. Yamagata, 2020b: Predictability of the Super IOD Event in 2019 and Its Link
- 430 With El Niño Modoki. *Geophys. Res. Lett.*, **47**, https://doi.org/10.1029/2019GL086713.
- Du, Y., Y. Zhang, L. Zhang, T. Tozuka, B. Ng, and W. Cai, 2020: Thermocline Warming Induced
- Extreme Indian Ocean Dipole in 2019. *Geophys. Res. Lett.*, **47**, 1–10,
- 433 https://doi.org/10.1029/2020GL090079.
- Feng, M., and G. Meyers, 2003: Interannual variability in the tropical Indian Ocean: A two-year time-
- scale of Indian Ocean Dipole. Deep. Res. Part II Top. Stud. Oceanogr., 50, 2263–2284,
- 436 https://doi.org/10.1016/S0967-0645(03)00056-0.
- Gadgil, S., P. V. Joseph, and N. V. Joshi, 1984: Ocean–atmosphere coupling over monsoon regions.
- 438 *Nature*, **312**, 141–143, https://doi.org/10.1038/312141a0.
- 439 —, P. N. Vinayachandran, P. A. Francis, and S. Gadgil, 2004: Extremes of the Indian summer
- monsoon rainfall, ENSO and equatorial Indian Ocean oscillation. *Geophys. Res. Lett.*, **31**, 2–5,
- 441 https://doi.org/10.1029/2004GL019733.
- Graham, N. E., and T. P. Barnett, 1987: Sea Surface Temperature, Surface Wind Divergence, and
- Convection over Tropical Oceans. Science (80-.)., 238, 657–659,
- https://doi.org/10.1126/science.238.4827.657.
- Gualdi, S., E. Guilyardi, A. Navarra, S. Masina, and P. Delecluse, 2003: The interannual variability in
- the tropical Indian Ocean as simulated by a CGCM. Clim. Dyn., 20, 567–582,
- 447 https://doi.org/10.1007/s00382-002-0295-z.
- Han, W., 2005: Origins and Dynamics of the 90-Day and 30–60-Day Variations in the Equatorial Indian
- Ocean. J. Phys. Oceanogr., **35**, 708–728, https://doi.org/10.1175/JPO2725.1.
- 450 —, T. Shinoda, L. L. Fu, and J. P. McCreary, 2006: Impact of atmospheric intraseasonal oscillations
- on the Indian Ocean dipole during the 1990s. J. Phys. Oceanogr., **36**, 670–690,

- 452 https://doi.org/10.1175/JPO2892.1.
- 453 —, and Coauthors, 2014: Intensification of decadal and multi-decadal sea level variability in the
- western tropical Pacific during recent decades. *Clim. Dyn.*, **43**, 1357–1379,
- 455 https://doi.org/10.1007/s00382-013-1951-1.
- 456 Hersbach, H., and Coauthors, 2019: *Global reanalysis: goodbye ERA-Interim, hello ERA5*. 17–24 pp.
- Horii, T., H. Hase, I. Ueki, and Y. Masumoto, 2008: Oceanic precondition and evolution of the 2006
- 458 Indian Ocean dipole. *Geophys. Res. Lett.*, **35**, https://doi.org/10.1029/2007GL032464.
- Huang, B., and J. L. Kinter III, 2002: Interannual variability in the tropical Indian Ocean. J. Geophys.
- 460 *Res.*, **107**, 3199, https://doi.org/10.1029/2001JC001278.
- 461 —, and J. Shukla, 2007a: Mechanisms for the interannual variability in the tropical Indian ocean. Part
- 462 II: Regional processes. *J. Clim.*, **20**, 2937–2960, https://doi.org/10.1175/JCLI4169.1.
- 463 —, and —, 2007b: Mechanisms for the Interannual Variability in the Tropical Indian Ocean. Part I:
- The Role of Remote Forcing from the Tropical Pacific. J. Clim., 20, 2917–2936,
- 465 https://doi.org/10.1175/jcli4151.1.
- Huang, B., Y. Xue, D. Zhang, A. Kumar, and M. J. McPhaden, 2010: The NCEP GODAS Ocean
- Analysis of the Tropical Pacific Mixed Layer Heat Budget on Seasonal to Interannual Time Scales.
- 468 *J. Clim.*, **23**, 4901–4925, https://doi.org/10.1175/2010JCLI3373.1.
- 469 —, and Coauthors, 2017: Extended reconstructed Sea surface temperature, Version 5 (ERSSTv5):
- 470 Upgrades, validations, and intercomparisons. J. Clim., 30, 8179–8205,
- 471 https://doi.org/10.1175/JCLI-D-16-0836.1.
- 472 Izumo, T., and Coauthors, 2010: Influence of the state of the Indian Ocean Dipole on the following
- 473 years El Niño. *Nat. Geosci.*, **3**, 168–172, https://doi.org/10.1038/ngeo760.
- 474 Ji, M., D. W. Behringer, and A. Leetmaa, 1998: An Improved Coupled Model for ENSO Prediction and
- Implications for Ocean Initialization. Part II: The Coupled Model. *Mon. Weather Rev.*, **126**, 1022–
- 476 1034, https://doi.org/10.1175/1520-0493(1998)126<1022:AICMFE>2.0.CO;2.
- Kiladis, G. N., J. Dias, K. H. Straub, M. C. Wheeler, S. N. Tulich, K. Kikuchi, K. M. Weickmann, and
- 478 M. J. Ventrice, 2014: A Comparison of OLR and Circulation-Based Indices for Tracking the MJO.
- 479 *Mon. Weather Rev.*, **142**, 1697–1715, https://doi.org/10.1175/MWR-D-13-00301.1.
- 480 Kripalani, R. H., and P. Kumar, 2004: Northeast monsoon rainfall variability over south peninsular India
- 481 vis-à-vis the Indian Ocean dipole mode. *Int. J. Climatol.*, **24**, 1267–1282,
- 482 https://doi.org/10.1002/joc.1071.

- 483 Krishnamurthy, V., and B. P. Kirtman, 2003: Variability of the Indian Ocean: Relation to monsoon and
- 484 ENSO. Q. J. R. Meteorol. Soc., **129**, 1623–1646, https://doi.org/10.1256/qj.01.166.
- Lau, N. C., and M. J. Nath, 2004: Coupled GCM simulation of atmosphere-ocean variability associated
- with zonally asymmetric SST changes in the tropical Indian Ocean. J. Clim., 17, 245–265,
- 487 https://doi.org/10.1175/1520-0442(2004)017<0245:CGSOAV>2.0.CO;2.
- Lawrence, D. M., and P. J. Webster, 2002: The Boreal Summer Intraseasonal Oscillation: Relationship
- between Northward and Eastward Movement of Convection. J. Atmos. Sci., **59**, 1593–1606,
- 490 https://doi.org/10.1175/1520-0469(2002)059<1593:TBSIOR>2.0.CO;2.
- 491 Li, T., B. Wang, C.-P. Chang, and Y. Zhang, 2003: A Theory for the Indian Ocean Dipole–Zonal
- 492 Mode*. J. Atmos. Sci., **60**, 2119–2135, https://doi.org/10.1175/1520-
- 493 0469(2003)060<2119:atftio>2.0.co;2.
- 494 Li, Z., W. Cai, and X. Lin, 2016: Dynamics of changing impacts of tropical Indo-Pacific variability on
- Indian and Australian rainfall. Sci. Rep., 6, 1–7, https://doi.org/10.1038/srep31767.
- Liebmann, B., and C. A. Smith, 1996: Description of a Complete (Interpolated) Outgoing Longwave
- 497 Radiation Dataset. *Bull. Am. Meteorol. Soc.*, **77**, 1275–1277, https://doi.org/10.2307/26233278.
- 498 Lim, Y., S.-W. Son, and D. Kim, 2018: MJO Prediction Skill of the Subseasonal-to-Seasonal Prediction
- 499 Models. J. Clim., **31**, 4075–4094, https://doi.org/10.1175/JCLI-D-17-0545.1.
- Lindzen, R. S., and S. Nigam, 1987: On the Role of Sea Surface Temperature Gradients in Forcing Low-
- Level Winds and Convergence in the Tropics. J. Atmos. Sci., 44, 2418–2436,
- 502 https://doi.org/10.1175/1520-0469(1987)044<2418:OTROSS>2.0.CO;2.
- Lu, B., and H. Ren, 2020: What Caused the Extreme Indian Ocean Dipole Event in 2019? *Geophys. Res.*
- 504 *Lett.*, **47**, 1–8, https://doi.org/10.1029/2020GL087768.
- 505 Luo, J.-J., W. Sasaki, and Y. Masumoto, 2012: Indian Ocean warming modulates Pacific climate
- 506 change. *Proc. Natl. Acad. Sci.*, **109**, 18701–18706, https://doi.org/10.1073/pnas.1210239109.
- Luo, J. J., R. Zhang, S. K. Behera, Y. Masumoto, F. F. Jin, R. Lukas, and T. Yamagata, 2010:
- Interaction between El Niño and extreme Indian Ocean dipole. J. Clim., 23, 726–742,
- 509 https://doi.org/10.1175/2009JCLI3104.1.
- Ma, S., C. Zhu, and J. Liu, 2020: Combined Impacts of Warm Central Equatorial Pacific Sea Surface
- Temperatures and Anthropogenic Warming on the 2019 Severe Drought in East China. *Adv. Atmos.*
- 512 *Sci.*, **37**, 1149–1163, https://doi.org/10.1007/s00376-020-0077-8.
- Madden, R. A., and P. R. Julian, 1971: Detection of a 40–50 Day Oscillation in the Zonal Wind in the

- Tropical Pacific. J. Atmos. Sci., 28, 702–708, https://doi.org/10.1175/1520-
- 515 0469(1971)028<0702:DOADOI>2.0.CO;2.
- McCreary, J. P., 1981: A linear stratified ocean model of the coastal undercurrent. *Philos. Trans. R. Soc.*
- 517 London. Ser. A, Math. Phys. Sci., 302, 385–413, https://doi.org/10.1098/rsta.1981.0176.
- McPhaden, M. J., S. E. Zebiak, and M. H. Glantz, 2006: ENSO as an integrating concept in earth
- science. *Science* (80-.)., **314**, 1740–1745, https://doi.org/10.1126/science.1132588.
- Meyers, G., P. McIntosh, L. Pigot, and M. Pook, 2007: The years of El Niño, La Niña and interactions
- with the tropical Indian Ocean. J. Clim., **20**, 2872–2880, https://doi.org/10.1175/JCLI4152.1.
- Murtugudde, R., J. P. McCreary, and A. J. Busalacchi, 2000: Oceanic processes associated with
- anomalous events in the Indian Ocean with relevance to 1997-1998. J. Geophys. Res. Ocean., 105,
- 524 3295–3306, https://doi.org/10.1029/1999JC900294.
- Rao, S. A., and T. Yamagata, 2004: Abrupt termination of Indian Ocean dipole events in response to
- intraseasonal disturbances. *Geophys. Res. Lett.*, **31**, L19306,
- 527 https://doi.org/10.1029/2004GL020842.
- Rayner, N. A., D. E. Parker, E. B. Horton, C. K. Folland, L. V. Alexander, D. P. Rowell, E. C. Kent, and
- A. Kaplan, 2003: Global analyses of sea surface temperature, sea ice, and night marine air
- temperature since the late nineteenth century. J. Geophys. Res., 108, 4407,
- 531 https://doi.org/10.1029/2002JD002670.
- Reynolds, R. W., N. A. Rayner, T. M. Smith, D. C. Stokes, and W. Wang, 2002: An improved in situ
- and satellite SST analysis for climate. *J. Clim.*, **15**, 1609–1625, https://doi.org/10.1175/1520-
- 534 0442(2002)015<1609:AIISAS>2.0.CO;2.
- Roeckner, E., and Coauthors, 1996: The atmospheric general circulation model ECHAM-4: model
- description and simulation of present-day climate. 171 pp.
- Saha, S., and Coauthors, 2014: The NCEP climate forecast system version 2. *J. Clim.*, **27**, 2185–2208,
- 538 https://doi.org/10.1175/JCLI-D-12-00823.1.
- Saji, N. H., and T. Yamagata, 2003: Possible impacts of Indian Ocean Dipole mode events on global
- climate. *Clim. Res.*, **25**, 151–169, https://doi.org/10.3354/cr025151.
- 541 Saji, N. H., B. N. Goswami, P. N. Vinayachandran, and T. Yamagata, 1999: A dipole mode in the
- tropical Indian Ocean. *Nature*, **401**, 360–363, https://doi.org/10.1038/43854.
- Saji, N. H., S. P. Xie, and T. Yamagata, 2006: Tropical Indian Ocean variability in the IPCC twentieth-
- 544 century climate simulations. J. Clim., 19, 4397–4417, https://doi.org/10.1175/JCLI3847.1.

- 545 Shinoda, T., H. H. Hendon, and M. A. Alexander, 2004: Surface and subsurface dipole variability in the
- Indian Ocean and its relation with ENSO. Deep. Res. Part I Oceanogr. Res. Pap., 51, 619–635,
- 547 https://doi.org/10.1016/j.dsr.2004.01.005.
- 548 Stuecker, M. F., A. Timmermann, F. F. Jin, Y. Chikamoto, W. Zhang, A. T. Wittenberg, E. Widiasih,
- and S. Zhao, 2017: Revisiting ENSO/Indian Ocean Dipole phase relationships. *Geophys. Res. Lett.*,
- 550 **44**, 2481–2492, https://doi.org/10.1002/2016GL072308.
- Vinayachandran, P. N., N. H. Saji, and T. Yamagata, 1999: Response of the equatorial Indian Ocean to
- an unusual wind event during 1994. *Geophys. Res. Lett.*, **26**, 1613–1616,
- 553 https://doi.org/10.1029/1999GL900179.
- Waliser, D. E., and N. E. Graham, 1993: Convective cloud systems and warm-pool sea surface
- temperatures: Coupled interactions and self-regulation. J. Geophys. Res., 98, 12881,
- 556 https://doi.org/10.1029/93JD00872.
- Wang, C., 2019: Three-ocean interactions and climate variability: a review and perspective. Clim. Dyn.,
- 53, 5119–5136, https://doi.org/10.1007/s00382-019-04930-x.
- Wang, G., W. Cai, K. Yang, A. Santoso, and T. Yamagata, 2020: A Unique Feature of the 2019 Extreme
- Positive Indian Ocean Dipole Event. *Geophys. Res. Lett.*, **47**, 1–9,
- 561 https://doi.org/10.1029/2020GL088615.
- Wang, H., A. Kumar, R. Murtugudde, B. Narapusetty, and K. L. Seip, 2019: Covariations between the
- Indian Ocean dipole and ENSO: a modeling study. Clim. Dyn., 53, 5743–5761,
- 564 https://doi.org/10.1007/s00382-019-04895-x.
- Webster, P. J., A. M. Moore, J. P. Loschnigg, and R. R. Leben, 1999: Coupled ocean–atmosphere
- dynamics in the Indian Ocean during 1997–98. *Nature*, **401**, 356–360,
- 567 https://doi.org/10.1038/43848.
- Xue, Y., M. Chen, A. Kumar, Z.-Z. Hu, and W. Wang, 2013: Prediction Skill and Bias of Tropical
- Pacific Sea Surface Temperatures in the NCEP Climate Forecast System Version 2. J. Clim., 26,
- 570 5358–5378, https://doi.org/10.1175/JCLI-D-12-00600.1.
- Yu, J. Y., Y. Zou, S. T. Kim, and T. Lee, 2012: The changing impact of El Nio on US winter
- temperatures. *Geophys. Res. Lett.*, **39**, https://doi.org/10.1029/2012GL052483.
- 573 Zhang, L., and W. Han, 2018: Impact of Ningaloo Niño on Tropical Pacific and an Interbasin Coupling
- Mechanism. *Geophys. Res. Lett.*, **45**, 11,300-11,309, https://doi.org/10.1029/2018GL078579.
- 575 —, —, K. B. Karnauskas, G. A. Meehl, A. Hu, N. Rosenbloom, and T. Shinoda, 2019: Indian

576	Ocean Warming Trend Reduces Pacific Warming Response to Anthropogenic Greenhouse Gases:
577	An Interbasin Thermostat Mechanism. Geophys. Res. Lett., 46, 10882-10890,
578	https://doi.org/10.1029/2019GL084088.
579	Zhu, J., B. Huang, A. Kumar, and J. L. Kinter III, 2015a: Seasonality in prediction skill and predictable
580	pattern of tropical Indian Ocean SST. J. Clim., 28, 7962-7984, https://doi.org/10.1175/JCLI-D-15
581	0067.1.
582	—, —, and J. L. Kinter, 2015b: Seasonality in prediction skill and predictable pattern of
583	tropical Indian Ocean SST. J. Clim., 28, 7962–7984, https://doi.org/10.1175/JCLI-D-15-0067.1.

Figure captions

Figure 1 Extreme pIODs during the satellite era. Sea surface temperature anomalies (SSTAs; °C) during September-November (SON; the peak season of IOD) in (a) 1994, (b) 1997, (c) 2006, and (d) 2019 from OISSTv2 data. White lines denote the -1 °C and 1 °C contours. Vectors represent surface wind anomalies (m s⁻¹). (e) Time evolution of the Dipole Mode Index (DMI; °C), defined as differences of SSTAs averaged over (50°E–70°E; 10°S–10°N) and (90°E–110°E; 10°S–EQ). The blue line is for ERSSTv5, red for HadISST and black for OISSTv2. (f) Evolution of monthly DMI (°C) from OISSTv2 during the extreme pIOD events in 1994 (orange), 1997 (red), 2006 (green), and 2019 (blue). The peak time (SON) of the four events are denoted by the vertical orange dashed lines in (e).

Figure 2 Evolution of the 2019 extreme pIOD. (a) Hovmöller diagram of daily surface zonal wind anomalies averaged between 15°N and 15°S from ERA-5 (m s⁻¹). (b) Daily SSTAs from OISSTv2 (°C) averaged between 10°N and 10°S. Contours in (b) represent 1°C or –1°C of SSTA. The vertical dashed lines in (a) and (b) denote 110°E and 130°E that represent the location of the Maritime Continent. (c) The daily DMI from OISSTv2.

Figure 3 (a) The three regions used to calculate the sea surface height (SSH) anomalies. In regions 1 and 3 (black and red dots), SSH is averaged meridionally, and in region 2 (blue dots), SSH is averaged in the direction perpendicular to the Sumatra coasts. (b) Evolution of SSH anomalies in the three regions denoted in (a). Unit is cm.

Figure 4 Mixed layer heat budget for the western (red; 50°E–70°E; 10°S–10°N) and eastern (blue; 90°E–110°E; 10°S–EQ) poles of the DMI. Shown are horizontal advection (Q_u), meridional advection (Q_v), vertical entrainment and diffusion (Q_w+Q_{zz}) and surface heat flux contributions (Q_q). Sums of these terms are also shown. Units are °C mon⁻¹. (a)-(f) Results from May to October 2019.

- Figure 5 Pentad mean OLR (shading; W m⁻²) and surface wind (vector; m s⁻¹) anomalies from April 26-607 608 June 4, 2019. 20-90 day filtered intraseasonal anomalies show very similar results. 609 **Figure 6** Same as Fig. 5, but for pentad-mean SST anomalies (°C). 610 Figure 7 Idealized SST forcing experiments. Idealized SST warming anomalies (shading; °C) and 611 simulated SON averaged surface wind anomalies (vector; m s⁻¹). The maximum SST warming 612 anomaly is 1 °C except for (d), in which the maximum warming is 2 °C. The forcing is centered 613 at (a) the CP-I, (b) the CP-II, (c) (d) the eastern equatorial Pacific (EP), (e) the western North 614 Pacific (WNP) and (f) the eastern North Pacific (ENP). Black vectors denote wind anomalies 615 that are statistically significant at the 90% confidence level. 616 Figure 8 SSH anomalies (shading; cm) in a linear ocean model forced with SON surface wind stress anomalies (vector; N m⁻²) in CP-I atmosphere model experiments relative to the control run. 617 618 Figure 9 CFSv2 predicted time evolution of monthly DMI (°C) of the 2019 extreme pIOD. Red curve is 619 the observations based on OISSTv2. Gray curves are 160-member ensemble of the 9-month prediction, and blue curve is the ensemble mean results. (a)–(i) are the predictions with January– 620 621 September initial conditions, respectively. 622 Figure 10 September SSTAs from CFSv2 forecasts with initial conditions in August 2019. Unit is °C. 623 Shown are results for the average of ensemble members that predict relatively (a) strong and (b) 624 weak pIODs. The strong and weak categories are selected as the 90th and 10th percentile of the simulated DMI, respectively (see Fig. 9i). (c) Differences between (a) and (b) that are statistically 625 626 significant at the 90% confidence level.
- Figure 11 Schematic diagram of the formation of the 2019 extreme pIOD. (a) At the initiation stage, the pIOD is triggered by easterly wind burst associated with a dry phase of the BSISO. (b) In the developing phase I (the Indian Ocean affects the Pacific Ocean), the MJO initiated in the tropical

Indian Ocean propagates eastward into the tropical Pacific, causing westerly wind anomalies in the central tropical Pacific. (c) developing phase II (the Pacific Ocean feedbacks on the Indian Ocean), the westerly wind anomalies lead to positive SSTAs in the central tropical Pacific, which in turn enhances the easterly wind anomalies over the equatorial Indian Ocean thorough the atmospheric bridge, contributing to the further amplification of the 2019 pIOD.

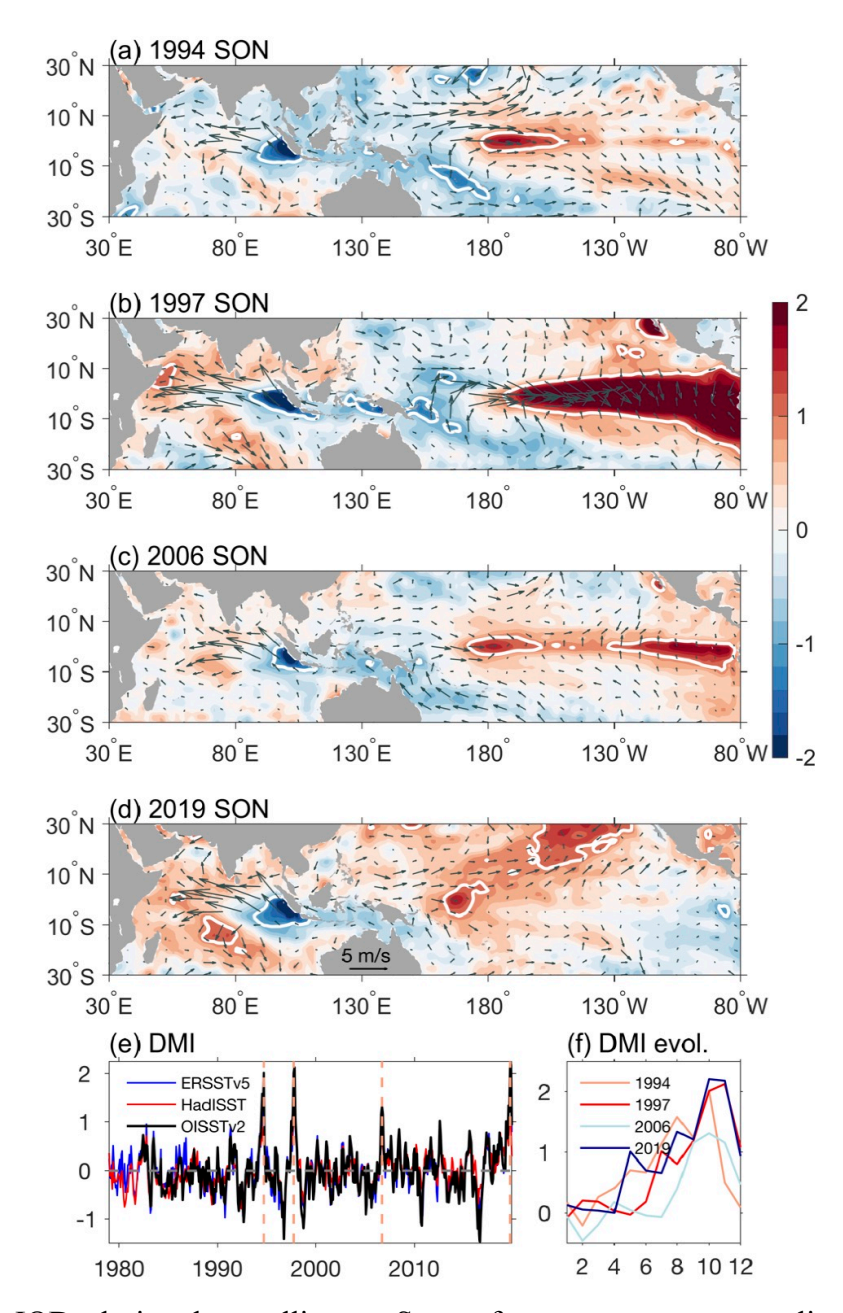


Figure 1 Extreme pIODs during the satellite era. Sea surface temperature anomalies (SSTAs; °C) during September-November (SON; the peak season of IOD) in (a) 1994, (b) 1997, (c) 2006, and (d) 2019 from OISSTv2 data. White lines denote the −1 °C and 1 °C contours. Vectors represent surface wind anomalies (m s⁻¹). (e) Time evolution of the Dipole Mode Index (DMI; °C), defined as differences of SSTAs averaged over (50°E−70°E; 10°S−10°N) and (90°E−110°E; 10°S−EQ). The blue line is for ERSSTv5, red for HadISST and black for OISSTv2. (f) Evolution of monthly DMI (°C) from OISSTv2 during the extreme pIOD events in 1994 (orange), 1997 (red), 2006 (green), and 2019 (blue). The peak time (SON) of the four events are denoted by the vertical orange dashed lines in (e).

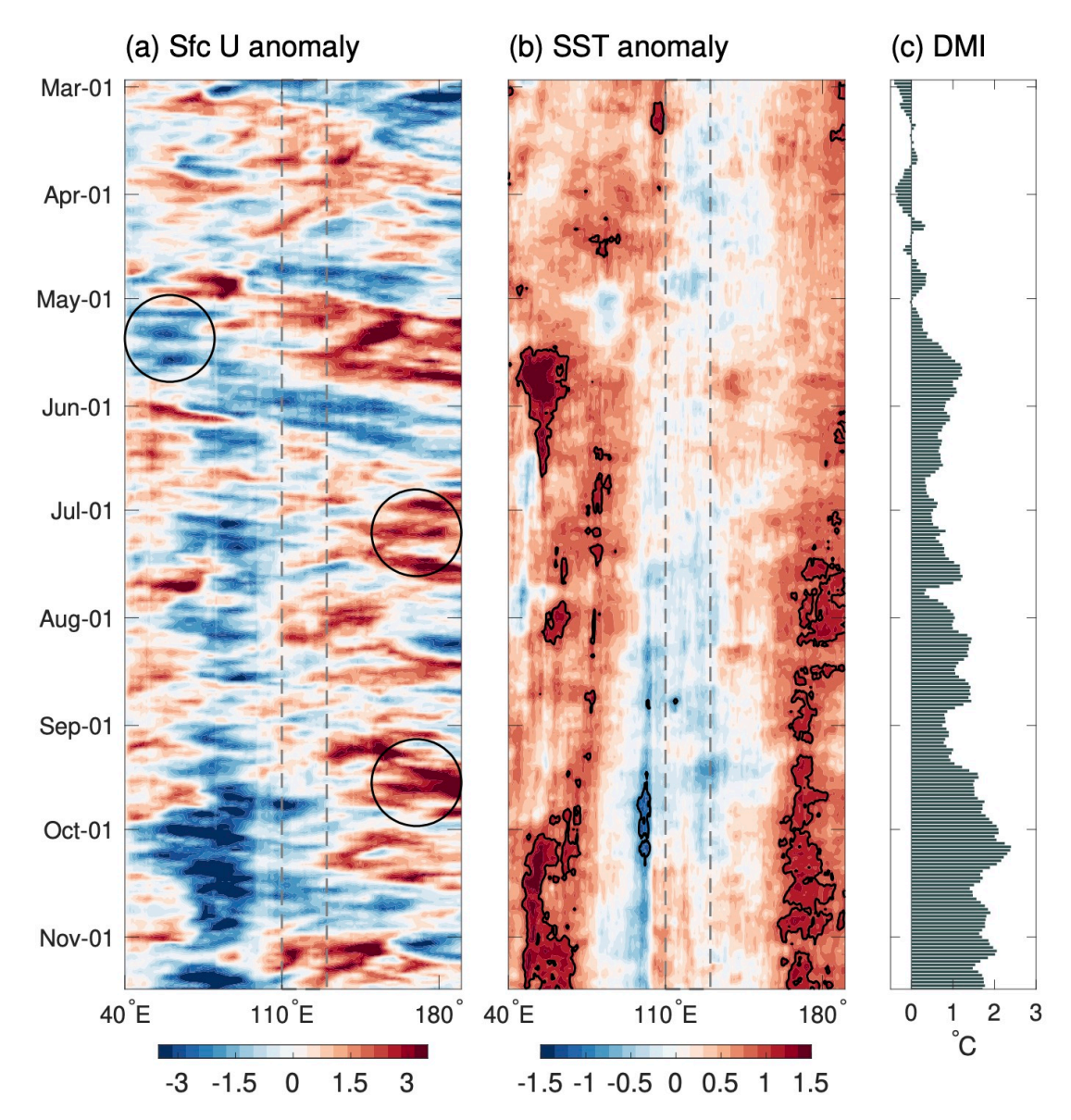


Figure 2 Evolution of the 2019 extreme pIOD. (a) Hovmöller diagram of daily surface zonal wind anomalies averaged between 15°N and 15°S from ERA-5 (m s⁻¹). (b) Daily SSTAs from OISSTv2 (°C) averaged between 10°N and 10°S. Contours in (b) represent 1°C or -1°C of SSTA. The vertical dashed lines in (a) and (b) denote 110°E and 130°E that represent the location of the Maritime Continent. (c) The daily DMI from OISSTv2.

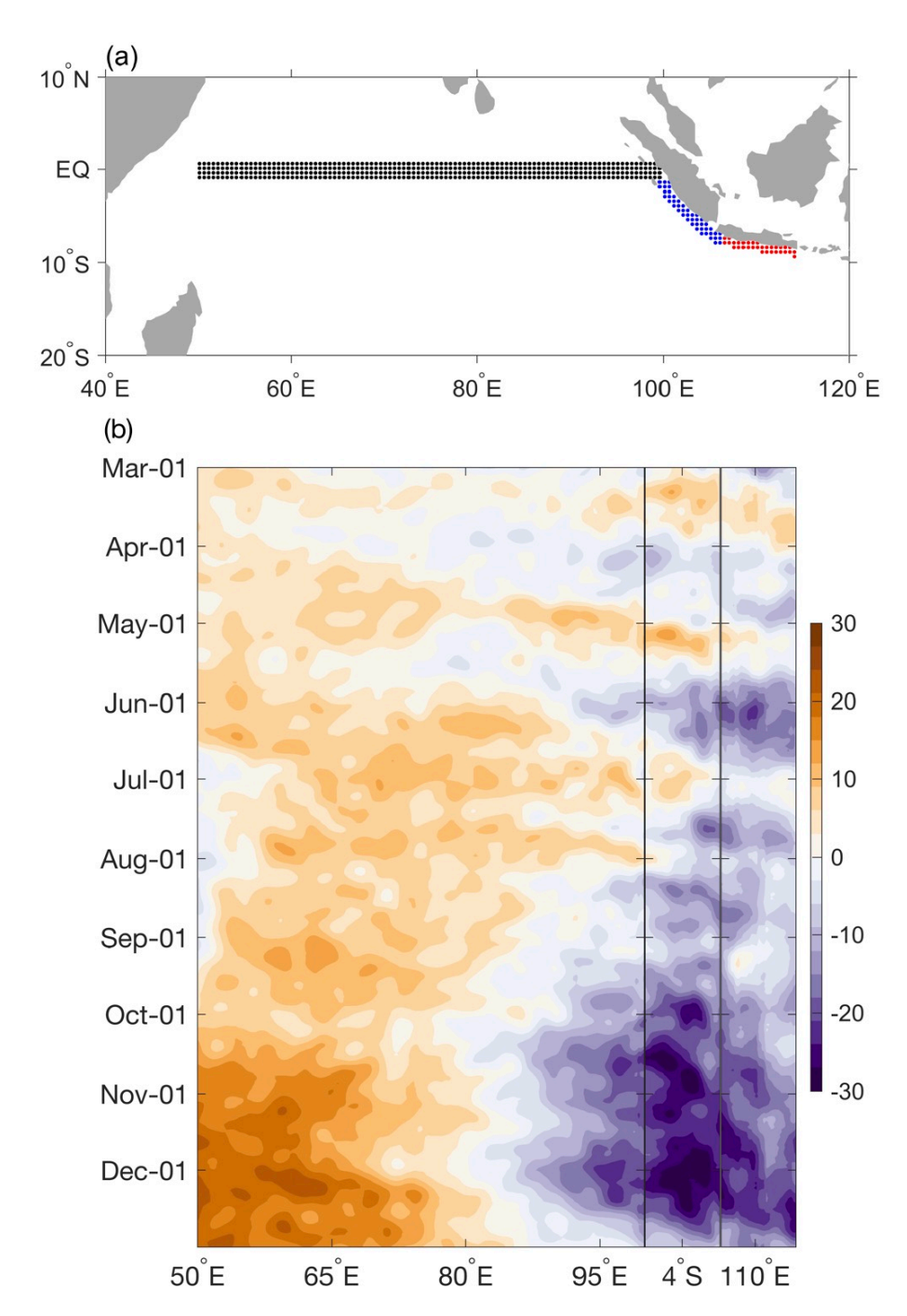


Figure 3 (a) The three regions used to calculate the sea surface height (SSH) anomalies. In regions 1 and 3 (black and red dots), SSH is averaged meridionally, and in region 2 (blue dots), SSH is averaged in the direction perpendicular to the Sumatra coasts. (b) Evolution of SSH anomalies in the three regions denoted in (a). Unit is cm.

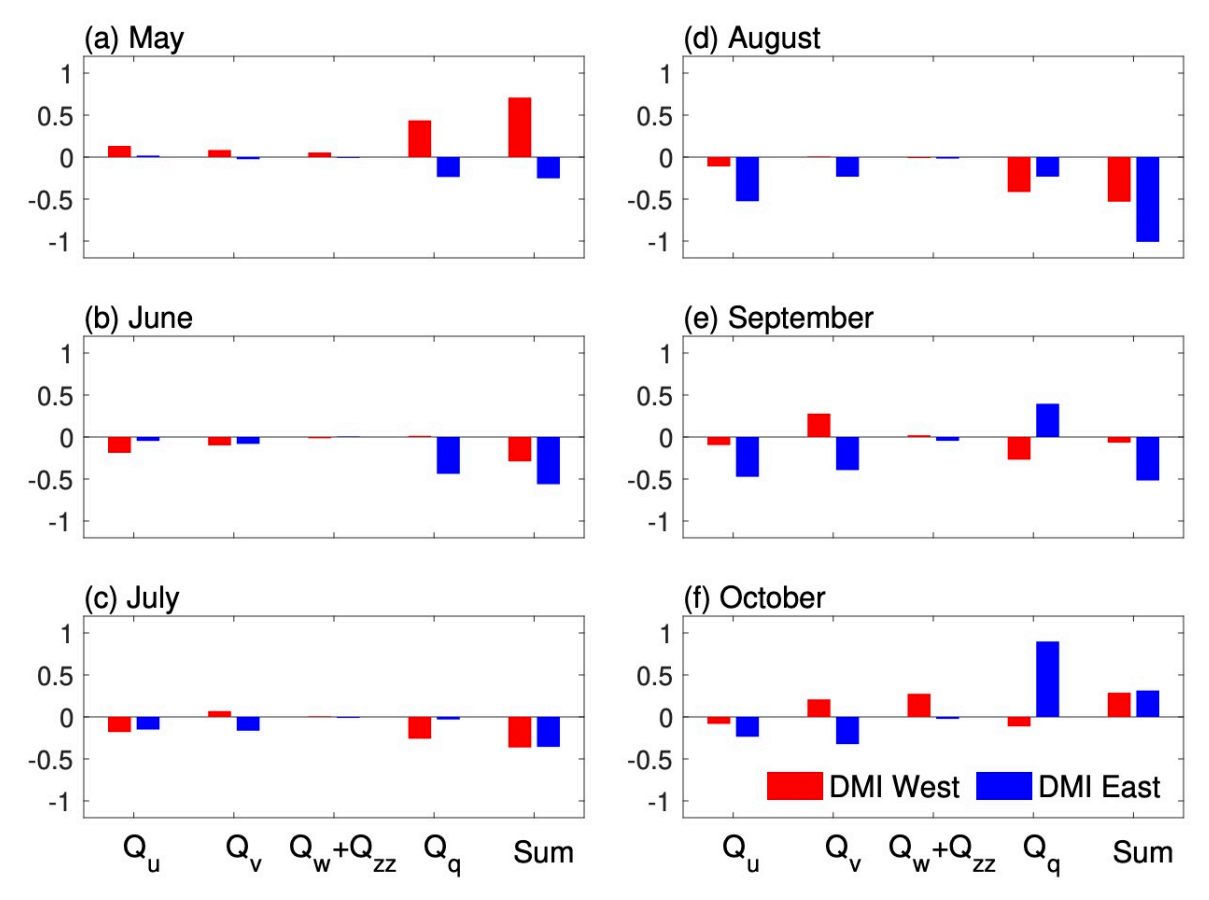


Figure 4 Mixed layer heat budget for the western (red; $50^{\circ}E-70^{\circ}E$; $10^{\circ}S-10^{\circ}N$) and eastern (blue; $90^{\circ}E-10^{\circ}E$; $10^{\circ}S-EQ$) poles of the DMI. Shown are horizontal advection (Q_u), meridional advection (Q_v), vertical entrainment and diffusion (Q_w+Q_{zz}) and surface heat flux contributions (Q_q). Sums of these terms are also shown. Units are ${}^{\circ}C$ mon⁻¹. (a)-(f) Results from May to October 2019.

2019 intraseasonal oscillation (late April-early June)

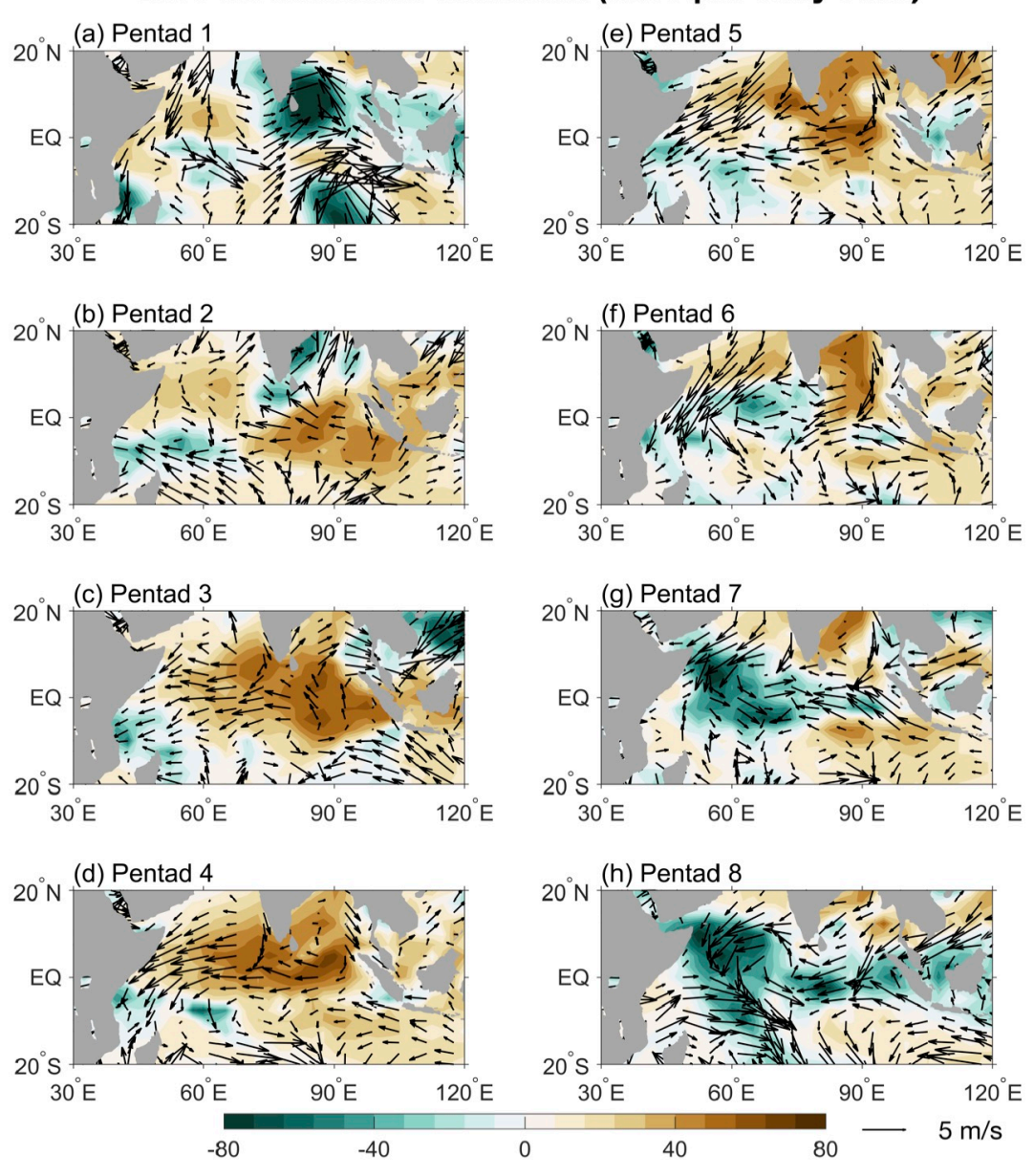


Figure 5 Pentad mean OLR (shading; W m⁻²) and surface wind (vector; m s⁻¹) anomalies from April 26-June 4, 2019. 20-90 day filtered intraseasonal anomalies show very similar results.

660661

2019 intraseasonal oscillation (late April-early June)

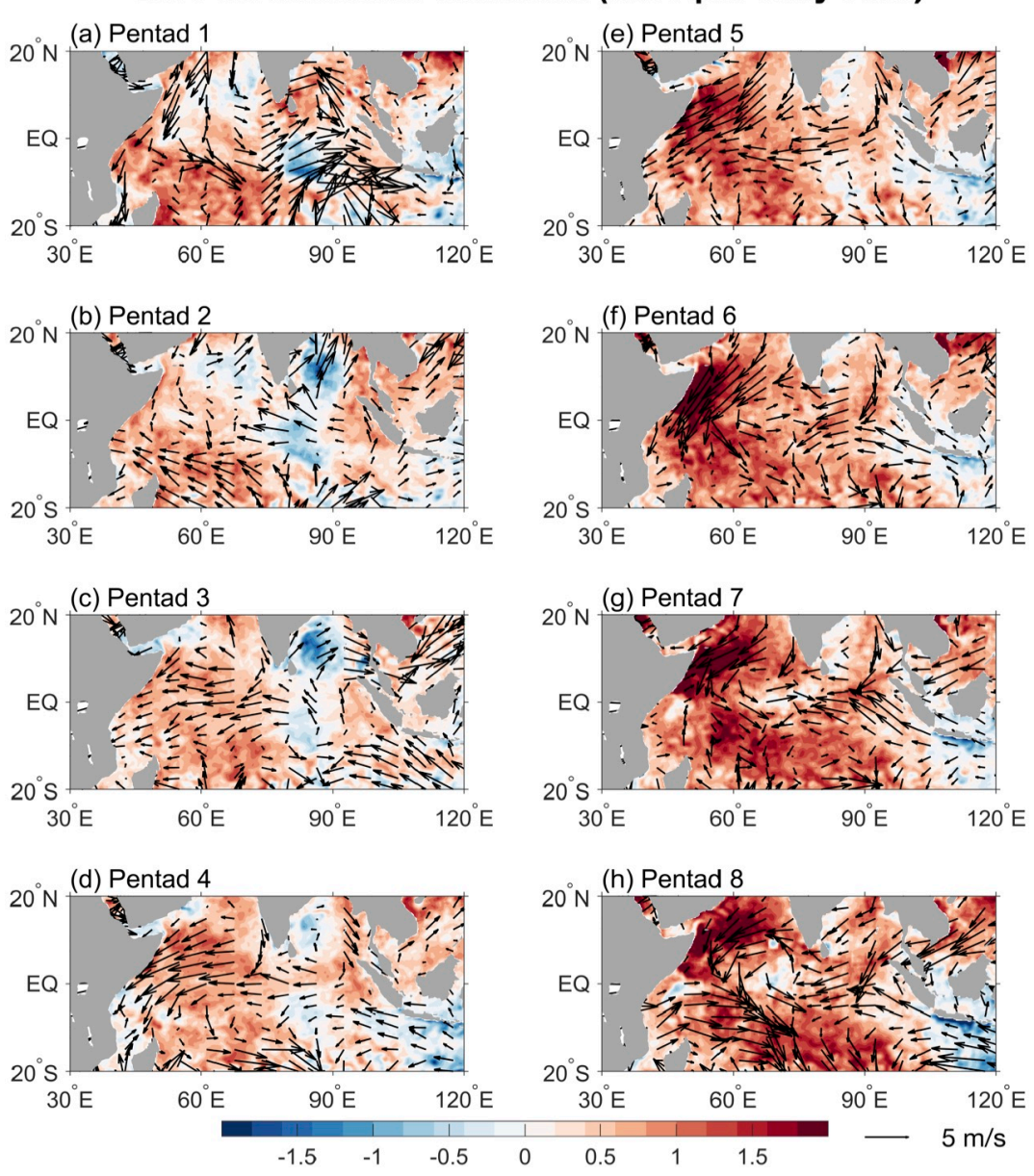


Figure 6 Same as Fig. 5, but for pentad-mean SST anomalies (°C).

SSTA & Sfc wind

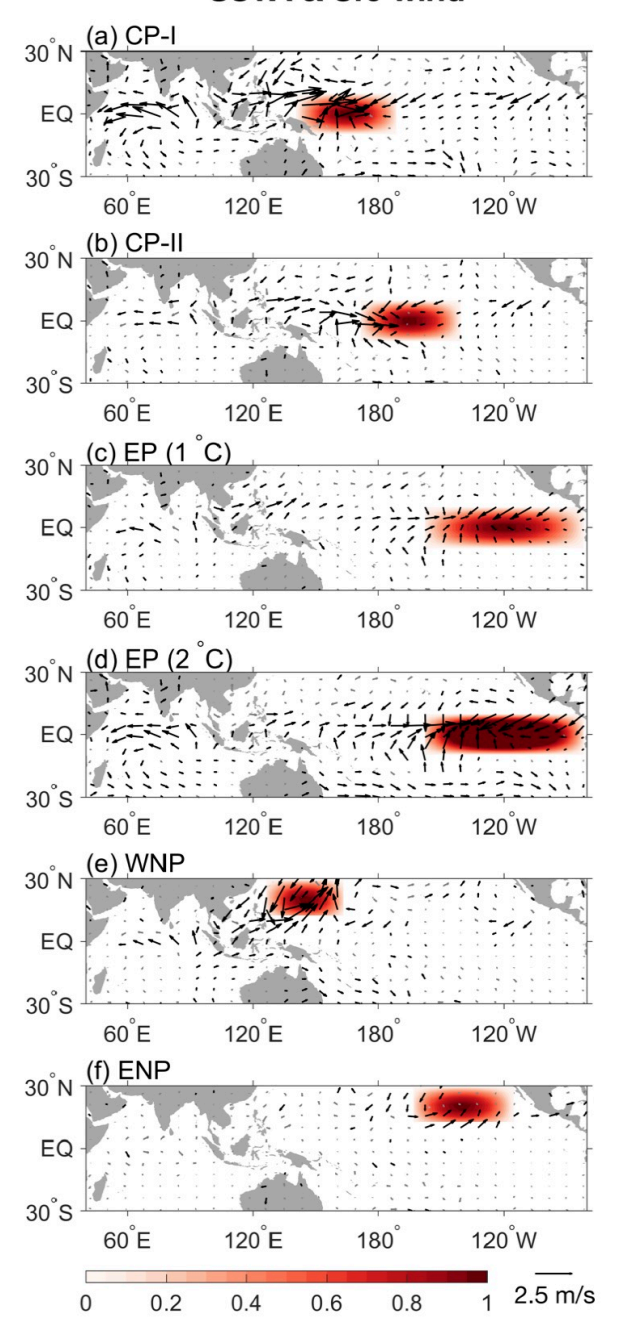


Figure 7 Idealized SST forcing experiments. Idealized SST warming anomalies (shading; °C) and simulated SON averaged surface wind anomalies (vector; m s⁻¹). The maximum SST warming anomaly is 1 °C except for (d), in which the maximum warming is 2 °C. The forcing is centered at (a) the CP-I, (b) the CP-II, (c) (d) the eastern equatorial Pacific (EP), (e) the western North Pacific (WNP) and (f) the eastern North Pacific (ENP). Black vectors denote wind anomalies that are statistically significant at the 90% confidence level.

SSH anomalies in linear ocean model

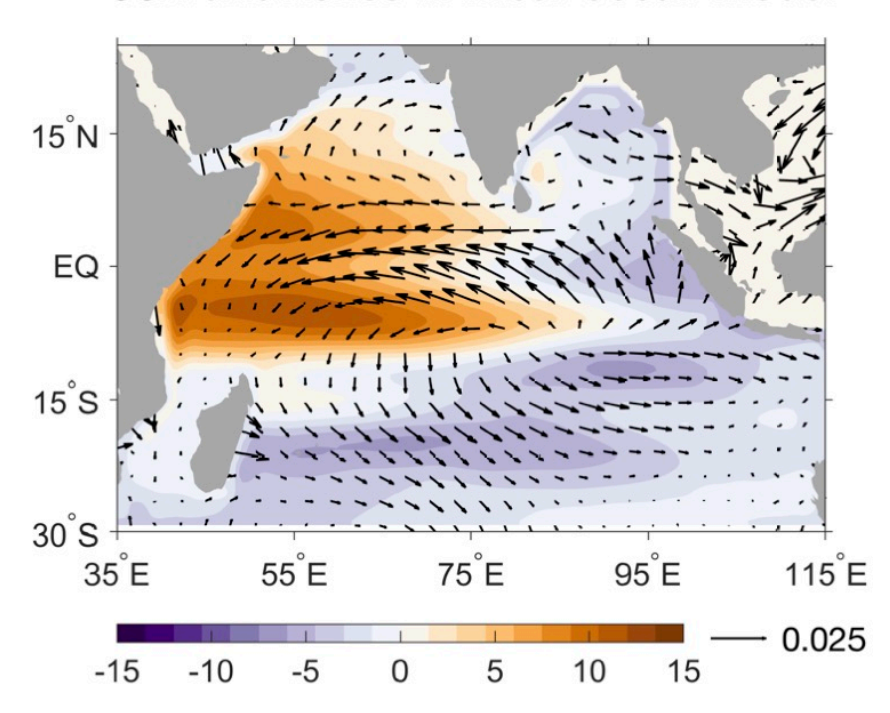


Figure 8 SSH anomalies (shading; cm) in a linear ocean model forced with SON surface wind stress anomalies (vector; N m⁻²) in CP-I atmosphere model experiments relative to the control run.

672673

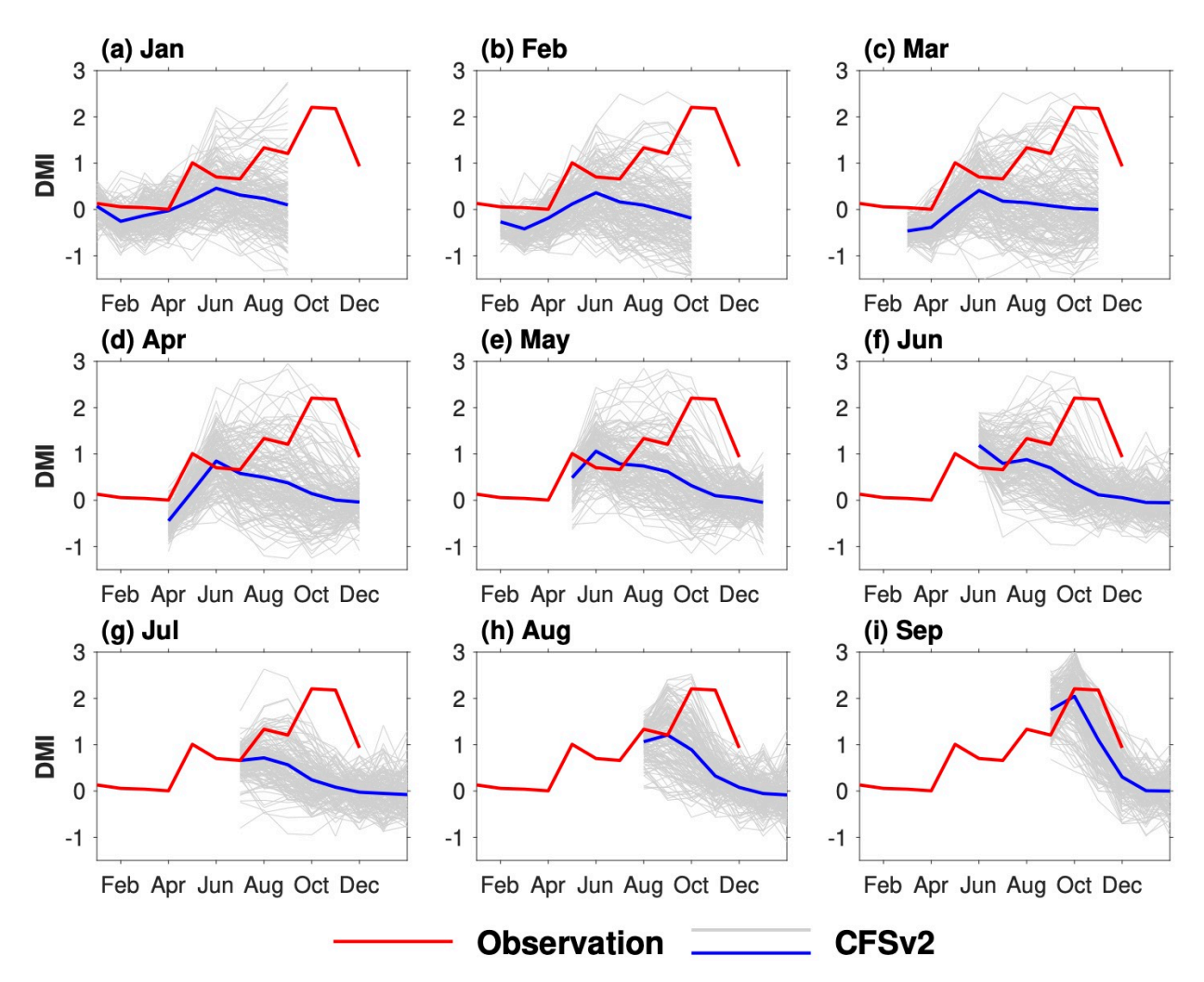


Figure 9 CFSv2 predicted time evolution of monthly DMI (°C) of the 2019 extreme pIOD. Red curve is the observations based on OISSTv2. Gray curves are 160-member ensemble of the 9-month prediction, and blue curve is the ensemble mean results. (a)–(i) are the predictions with January–September initial conditions, respectively.

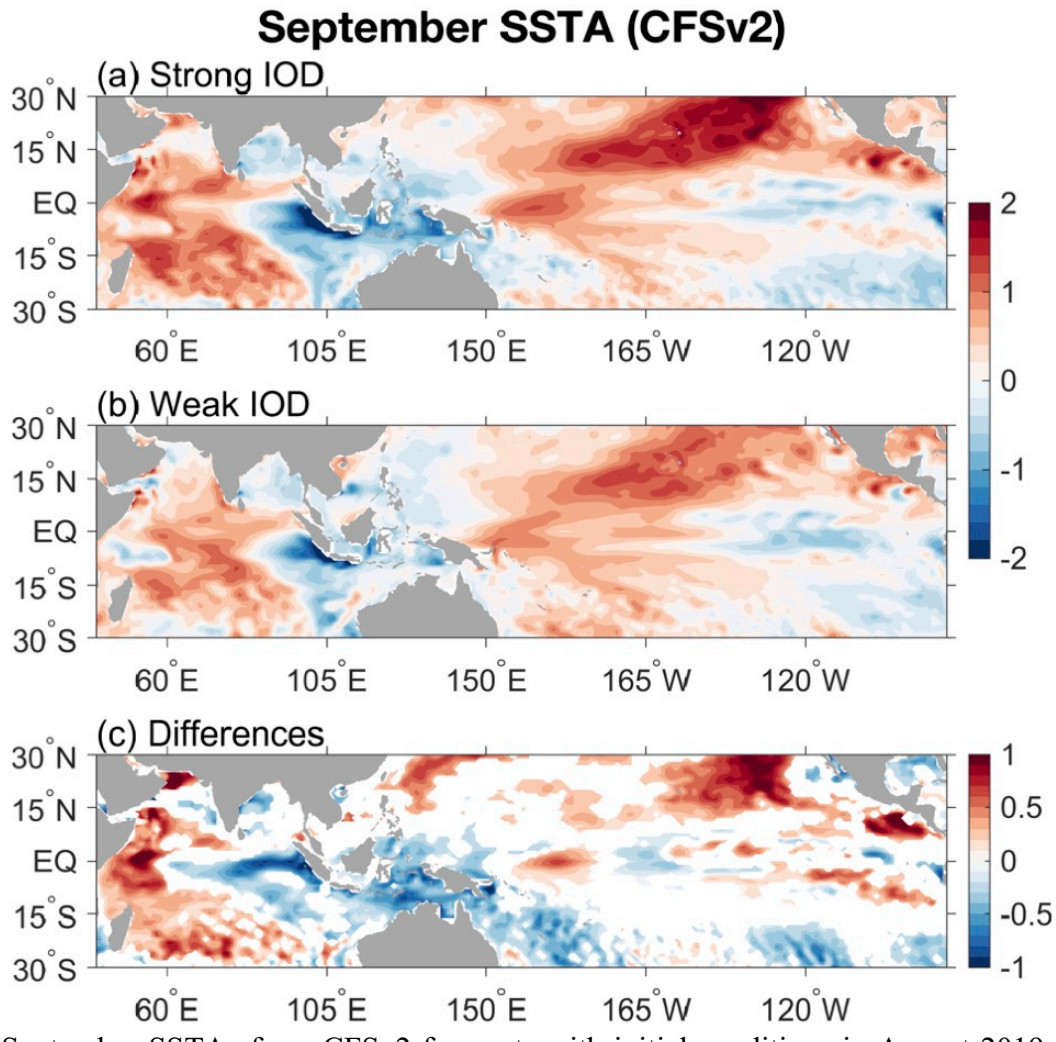
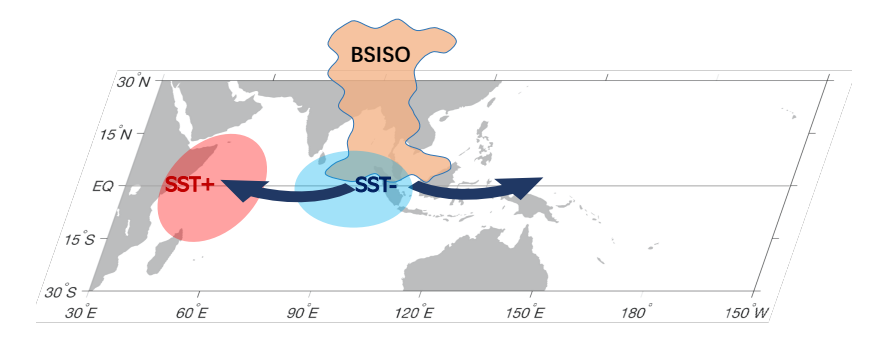
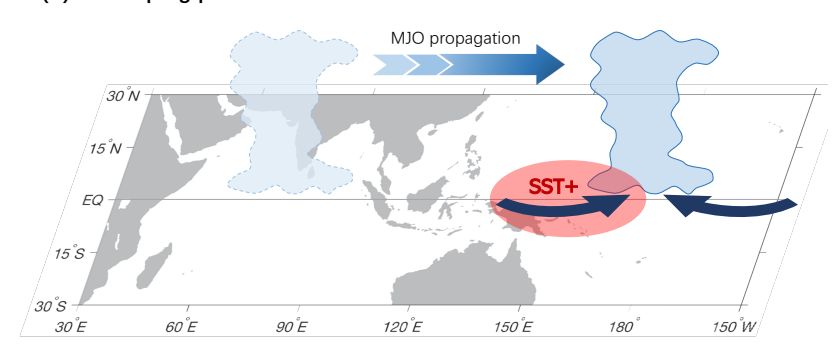


Figure 10 September SSTAs from CFSv2 forecasts with initial conditions in August 2019. Unit is °C. Shown are results for the average of ensemble members that predict relatively (a) strong and (b) weak pIODs. The strong and weak categories are selected as the 90th and 10th percentile of the simulated DMI, respectively (see Fig. 9i). (c) Differences between (a) and (b) that are statistically significant at the 90% confidence level.

(a) Initiation: Easterly wind bursts



(b) Developing phase I: the Indian Ocean affects Pacific Ocean



(c) Developing phase II: the Pacific Ocean feedback on Indian Ocean

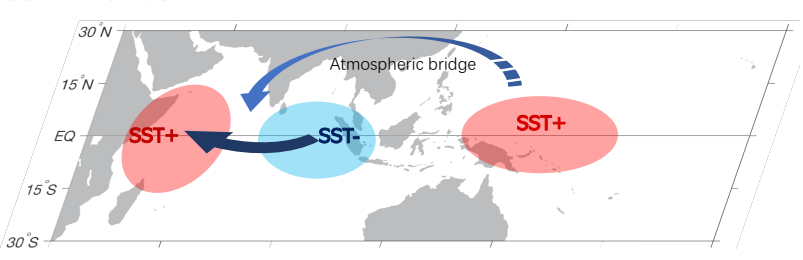


Figure 11 Schematic diagram of the formation of the 2019 extreme pIOD. (a) At the initiation stage, the pIOD is triggered by easterly wind burst associated with a dry phase of the BSISO. (b) In the developing phase I (the Indian Ocean affects the Pacific Ocean), the MJO initiated in the tropical Indian Ocean propagates eastward into the tropical Pacific, causing westerly wind anomalies in the central tropical Pacific. (c) developing phase II (the Pacific Ocean feedbacks on the Indian Ocean), the westerly wind anomalies lead to positive SSTAs in the central tropical Pacific, which in turn enhances the easterly wind anomalies over the equatorial Indian Ocean thorough the atmospheric bridge, contributing to the further amplification of the 2019 pIOD.